Phase field model of faceted anatase TiO2 dendrites in low pressure chemical vapor deposition

Applied Physics Letters

Phase field model of faceted anatase TiO_2 dendrites in low pressure chemical vapor deposition

Cite as: Appl. Phys. Lett. **119**, 221602 (2021); https://doi.org/10.1063/5.0071731
Submitted: 16 September 2021 • Accepted: 11 November 2021 • Published Online: 30 November 2021

Y. Huang, S. L. Masters, S. P. Krumdieck, et al.

Applied Physics Letters ARTICLE scitation.org/journal/apl

Phase field model of faceted anatase TiO_2 dendrites in low pressure chemical vapor deposition

Cite as: Appl. Phys. Lett. **119**, 221602 (2021); doi: 10.1063/5.0071731
Submitted: 16 September 2021 · Accepted: 11 November 2021 ·
Published Online: 30 November 2021

Y. Huang,[1,a] S. L. Masters,[2] S. P. Krumdieck,[3] and C. M. Bishop[1]

AFFILIATIONS

[1]Department of Mechanical Engineering, University of Canterbury, Christchurch 8140, New Zealand
[2]School of Physical and Chemical Sciences, University of Canterbury, Christchurch 8140, New Zealand
[3]School of Energy, Geoscience, Infrastructure and Society, Heriot-Watt University, Edinburgh, United Kingdom

[a]Author to whom correspondence should be addressed: yicun.huang@pg.canterbury.ac.nz

ABSTRACT

Anatase TiO_2 nanorods with a well-defined ⟨110⟩ texture have been studied using a model-based characterization technique based on a previous modeling framework. Intricate secondary side facet characteristics of tilt angles of 26.5° have been indexed, and a ⟨112⟩ growth direction of the well-aligned facets is identified. These results have not been accessed experimentally but crucial in understanding the nature of the most abundant facets and their structural properties. We find agreement between our results and indirect experimental measurements. Highly exposed {116} facets are found to be responsible for excellent electrochemical surface properties in nanostructured anatase TiO_2 thin films.

Polycrystalline titania thin films with nanorod morphology have been engineered to match desired microstructures in applications such as antimicrobial coatings,[1,2] template synthesis,[3] and solar cells.[4–6] The excellent photoconductive property[7] pertinent to these applications was attributed to the unique dendrite-like morphology with high porosity developed during chemical vapor deposition (CVD). Unlike TiO_2 epitaxial films or particles, these rapidly grown fiber-textured nanorods adopted out-of-equilibrium shapes that are fundamentally different from the usual {101}-terminated morphologies. Multifaceted, secondary dendritic structures are formed under low-pressure conditions, and they are inclined at an angle with respect to the fastest growth direction of the nanorods at the late stage of the thickness growth.[8,9] Focused ion-beam has helped to isolate such a single-crystalline nanorod structure, and scanning electron microscopy (SEM) has been used to examine the dendritic morphology.[10]

Anatase and rutile are the two major polymorphs commonly synthesized in TiO_2 nanorod films. Several studies using x-ray diffraction analysis (XRD) and selected area electron diffraction (SAED) have confirmed the ⟨001⟩ fiber texture for rutile[3] and ⟨110⟩ for anatase nanorods.[8–15] Anatase is generally considered a better photocatalyst than rutile owing to its higher surface-adsorption rates[16] and faster exciton transport to the surface.[17] While there has been an agreement on the ⟨110⟩ texture of anatase TiO_2 (A-TiO_2) nanorods, the identification of all surface facets is still an open question due to challenging sample preparation of the complex dendritic morphology. Recently, *in situ* liquid transmission electron microscopy (TEM) of photocatalytic rutile nanorods was demonstrated, where evolved gas bubble frequency varied by facet for simple geometries with dimensions on the order of 50 nm.[18] Atomic force microscopy based methods,[19] for examples, also require relatively simple geometries to study facet orientation effects.

Dendritic structures have been extensively studied in applications such as catalysts[20] and batteries,[21] whose growth morphology is dependent on the materials and processing conditions. Numerous growth mechanisms of A-TiO_2 nanorods, leading to different exposed surfaces, have been proposed based on indirect observations on isolated nanorods. Jung *et al.* used the theory of competitive growth for polycrystalline thin films to explain the nanorod morphology,[12,14] which results in low-energy facets by the assumption that the surface diffusion is not the rate limiting process. It is, hence, inadequate to explain the branching of secondary facets and their alignment. In a TEM analysis, {112} and {001}-facets were identified indirectly using SAED to be the most abundant facets of A-TiO_2 nanorods, and their presence was explained by the growth mechanism of oriented

attachment.[8] However, the theory of oriented attachment in self-assembly and coarsening of nano-particles cannot properly describe the kinetically grown nanorods during vapor deposition processes. Alternative theories have attributed the multi-faceted nanorod morphology to the specific CVD techniques used in the fabrication[10,15,22] without giving a detailed analysis of the resulting morphology.

Despite the different techniques used in fabricating A-TiO_2 nanorods with the characteristic multi-faceted morphology, the only common processing parameter among these deposition techniques is the vapor pressure, being in the range of 100–150 Pa.[8,10,12,13] Therefore, it is reasonable to expect that the nanorod morphology is induced by the unstable crystal growth under low vapor pressure during CVD. Vapor pressure is crucial in determining the mass transport of species to the surface. A rough estimate shows that the mean free path is on the order of 100 μm for the reported CVD methods, which yields a Knudsen number on the order of 100 as far as the diameter of the nanorod is concerned,[23] typically under 1 μm. This implies that the mass transport is ballistic at the scale of depositing nanorod surfaces. Under this transport regime, ballistic induced shadowing growth is expected.[24–26] Furthermore, surface diffusion plays an important role in the development of the multi-faceted morphology.

Existing theories of morphological development of films arisen from the interplay between the surface diffusion and shadowing growth are limited to the case of the isotropic surface flux.[27–32] Nevertheless, the growth of realistic materials with a 3D multi-faceted morphology is often considered to be dominated by strongly anisotropic surface energies.[33] In the previous work, we proposed a phase field model incorporating detailed treatments of both process-specific shadowing growth and faceting driven by anisotropic surface energies to study the morphology of nanorods grown by oblique angle deposition.[34] It was found that the film morphology is influenced not only by the uni-directional flux due to ballistic transport but also by the strength of adparticle mobility in relation to asymmetric surface diffusion. We showed that shadowing and directional sticking coefficients were important for growing films with abnormal columnar tilting observed experimentally in two cubic crystals, MgO and CaF_2.

In this Letter, we build on our previous work on uni-directional deposition to generalize to low pressure CVD, and we study the development of A-TiO_2 nanorod morphologies. The model and its implementation for a tetragonal crystal symmetry are presented. We report the surface index of dendritic facets developed from a distorted columnar rod below the top of a growing nanorod during its thickness growth stage. We show that a characteristic dendritic morphology is obtained for low ratios of adparticle mobility to the ballistic flux in CVD.

In our previous work, a continuum model was formulated that describes an interfacial growth problem posed by two competing effects, i.e., the protuberances formed on the solid-gas interface following the ballistic trajectories of ad-particles and the stabilizing capillary forces due to surface diffusion.[34] The solid phase and the gas phase are treated as superimposed continua using the thermodynamically consistent diffuse-interface theory. Particle-size effects are ignored, because very little of the complex chemistry involved in CVD is known.

To take account for the trajectories of the incoming flux characteristic of a CVD process, we modify and introduce here a matrix of the vapor field $g_{\theta,\psi}(\boldsymbol{r},t)$. It is parameterized by the polar angle θ and azimuthal angle ψ, each associated with a unique rain vector $\vec{R}_{\theta,\psi}$, defined in Eq. (1). The direction of $\vec{R}_{\theta,\psi}$ is specified by θ and ψ, and its magnitude is equal to $|\vec{R}|$. The typical ranges of the two angles for CVD, i.e., $0^\circ < \theta < 90^\circ$ and $0^\circ < \psi < 360^\circ$, are considered

$$\vec{R}_{\psi,\theta} = |\vec{R}| \cdot \begin{bmatrix} \cos\psi & 0 & \sin\psi \\ 0 & 1 & 0 \\ -\sin\psi & 0 & \cos\psi \end{bmatrix} \begin{bmatrix} 0 \\ -\sin(\theta) \\ -\cos(\theta) \end{bmatrix}. \quad (1)$$

A suitable coordinate system for ⟨110⟩-textured nanorods is chosen so that the position vector $\boldsymbol{r}$ is a linear combination of three orthogonal unit vectors having the same crystallographic directions as [1 1 0], [0 0 1], and [$\bar{1}$ 1 0] of A-TiO_2. The crystallographic reference axes and the geometry of rain vectors are illustrated in Fig. 1. The ballistic trajectories of the ad-particles follow an angular cumulative distribution function[35] $\mathcal{P}(\theta)$ that is often modeled by Maxwellian distributions determined by different CVD reactor setups.[36] For generality in our modeling approach, we assume a simple cosine law[37] $d\mathcal{P}/d\theta = \cos(\theta)$.

Based on the previous growth model[34] and by considering the ballistic flux distribution, we propose a formulation describing the transport of materials to the interface as well as the subsequent consumption and redistribution by surface diffusion. The first term in Eq. (2) describes the diffusional processes of the interface driven by the ad-particle mobility with coefficient M. The functional derivative of the surface free energy $F[\phi]$ is minimized during the time evolution of the conservative phase field $\phi(\boldsymbol{r},t)$ with equilibrium values $\phi = 1$ in the solid and $\phi = -1$ in the vapor. The second term captures the arrival of the material flux onto the solid-vapor interface defined by $\phi = 0$. The incorporation of ad-particles into the interface is modeled by the acceptance function $\mathcal{A}_{\theta,\psi}$, integrated over all possible angles of incidence. The ballistic transport is modeled by the advection of the vapor field $g_{\theta,\psi}(\boldsymbol{r},t)$ in Eq. (3) with the second term accounting for the shadowing effect using a conversion term with coefficient B sufficiently large and arbitrarily chosen to ensure $g = 0$ in the solid

$$\frac{\partial\phi}{\partial t} = M\nabla^2\frac{\delta F}{\delta\phi} + (\nabla\phi)^2\int_0^{2\pi}\int_0^{\frac{\pi}{2}}\mathcal{A}_{\theta,\psi}\, g_{\theta,\psi}\, d\theta d\,\psi\ , \quad (2)$$

$$\frac{\partial g}{\partial t} = -\vec{R}_{\theta,\psi}\cdot\nabla g - B(\nabla\phi)^2 g. \quad (3)$$

We define an acceptance function[38] in Eq. (4) to take account of the flux distribution of a general CVD process, where $\boldsymbol{n}(\boldsymbol{r}) = -\nabla\phi/|\nabla\phi|$ is the outward pointing, unit normal to the ϕ level set

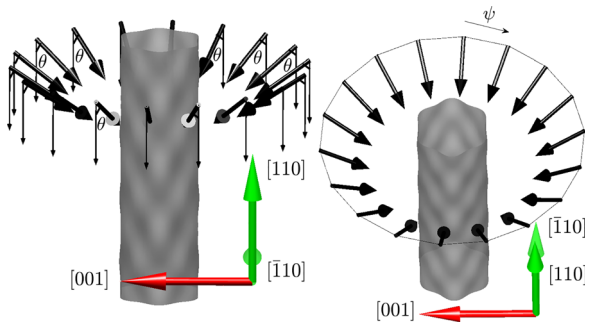

FIG. 1. Geometry of an infinite cylinder periodic in [1 1 0] with a range of rain vectors $\vec{R}_{\theta,\psi}$ represented by the arrows.

$$\mathcal{A}_{\theta,\psi}(\vec{n},\vec{R}_{\theta,\psi}) = \frac{d\mathcal{P}}{d\theta}\,|\vec{R}_{\theta,\psi}\times\vec{n}|. \tag{4}$$

In order to account for the highly anisotropic morphology found in A-TiO_2 nanorods, we employ a regularized free energy functional $F[\phi]$ that incorporates the sharp edges and corners naturally. The formulations and applications of this functional have been established in the literature.[33,39–41] The value of $F[\phi]$ depends on the non-dimensional surface free energy density $\gamma(\boldsymbol{n})$ constructed facet-wise using the formula[33] shown as

$$\gamma(\boldsymbol{n}) = 1 - \sum_{i=1}^{m} a_i(\boldsymbol{m}_i\cdot\boldsymbol{n})^{\omega_i}\Theta(\boldsymbol{m}_i\cdot\boldsymbol{n}), \tag{5}$$

where a_i and ω_i set the relative depth and width of the energy minima, respectively, and the $\Theta(\boldsymbol{m}_i\cdot\boldsymbol{n})$ term excludes the opposite orientations that may not be crystallographically equivalent. We note here that this construction is material-specific. It means for A-TiO_2 that the facet orientations in tetragonal symmetry need to be converted to Cartesian coordinates before plugging them into Eq. (5). In addition, this simple construction of a 3D energy density function is tunable to a finite number of facets m, specified by families of equivalent facets with orientation $\boldsymbol{m}_i$. For accuracy of the growth dynamics, it is important to identify the families of facets, apart from the common {001}, {100}, and {101}, that are most relevant to the growth of the multi-faceted morphology observed.

To this end, we turn to the characterization that identified a 90° angle between the orientation of the bounding facets of secondary plates and the fastest growth direction of these well-aligned structures.[9,13] For a realistic description of the surface energies of A-TiO_2, we include in the construction of $\gamma(\boldsymbol{n})$ the pairs of orientations $\boldsymbol{m}_i \perp \boldsymbol{m}_j$. A systematic search is undertaken for low index facets with $\boldsymbol{m}_i^2 \le 50$ with tolerance ±2°, and these pairs are joined graphically on the pole figures shown in Fig. 2. It includes pairs from the {103}-{112} (black), {112}-{116} (blue), and {101}-{116} (red) families forming 91.2°, 91.3°, and 91.0° angles, respectively. For simplicity, the trivial $\boldsymbol{m}_{\{101\}} \perp \boldsymbol{m}_{\{001\}}$ pairs are not drawn on the pole figure.

The *ab initio*-derived surface energy values[23] $\gamma_{\{001\}} = 0.78$, $\gamma_{\{100\}} = 0.45$, $\gamma_{\{101\}} = 0.35$, $\gamma_{\{103\}} = 0.66$, $\gamma_{\{112\}} = 0.73$, and $\gamma_{\{116\}} = 0.75\ \mathrm{J\,m^{-2}}$ of anatase are used for construction of γ. In Fig. 3, facet-specific coloring according to the inverse pole figure (IPF) stereographic triangle of anatase is used to visualize the equilibrium shape of a A-TiO_2 particle obtained with the constructed $\gamma(\boldsymbol{n})$ function. The corresponding γ-plot, i.e., $\boldsymbol{n}\gamma(\boldsymbol{n})$, is superimposed in gray on the particle, which is the convex envelope of the γ-plot and coincides with the particle shape developed by an energy minimization calculation. This Wulff shape agrees with the accepted equilibrium shape of anatase nanoparticles, which is dominated by {101} surfaces.[42]

Growth is modeled by the deposition flux $\nabla g_{\theta,\psi}(\boldsymbol{r},t)$ and the incorporation of the g field onto the interface region $(\nabla\phi)^2$. Each vapor field $g_{\theta,\psi}$ is characterized by its rain vectors $\vec{R}_{\theta,\psi}$, all with magnitude $|\vec{R}|$. The interfacial morphology is frequently considered to result from the interplay between the deposition flux and the diffusive mobility of the material interface.[28,30,32] We consider in our formulation a ratio between the mobility coefficient and the magnitude of the flux $M/|\vec{R}|$. This ratio is varied for different simulations.

From the experimental works of microscopy characterizations, it is evident that the most abundant facets are found below the tip of the nanorod.[8,9] For this reason, an infinite cylindrical geometry periodic in [1 1 0] is used for the simulation of nanorods. In particular, a periodic cylinder with radius $r = 0.3 + \delta\cos(6\psi)\cos(8\pi z) + \delta_{\langle 001\rangle}\cos(\psi)\cos(4\pi z)$ is chosen for the initialization of the phase field. This distorted cylinder with average radius 0.3 is obtained by the superposition of an arbitrary distortion of amplitude $\delta = 0.02$ and a major distortion toward ⟨001⟩ with amplitude $\delta_{\langle 001\rangle} = 0.1$, all normalized by the dimension of the simulation cell. For the four lateral boundaries in [$\bar{1}$ 1 0] and [0 0 1] directions, no-flux boundary conditions are applied

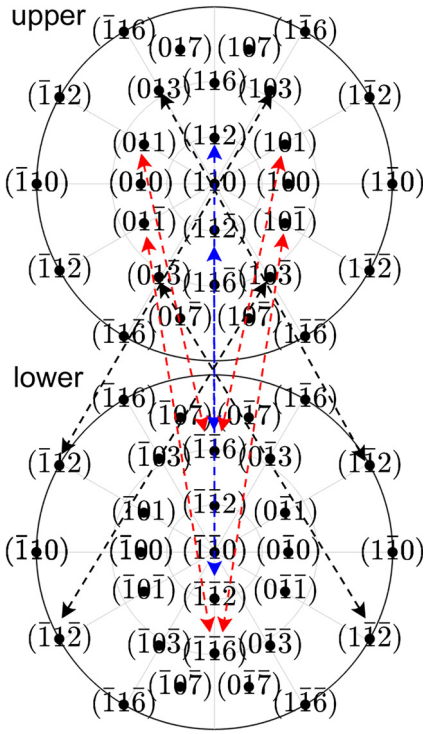

FIG. 2. Pole figures showing the possible pairs of orientations of the most abundant facets and their fastest growth direction that are 90°±2° apart. Here, high-index facets considered are limited up to {107}.

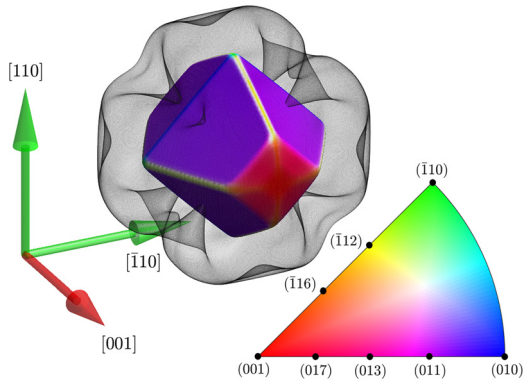

FIG. 3. The equilibrium shape of A-TiO_2 particles and the $\gamma(\boldsymbol{n})$-plot of interfacial energy corresponding to Eq. (5) in gray.

to Eq. (2) an in-ow boundary condition $g = 1$ is applied to Eq. (3) for a constant supply of vapor. Periodic boundary conditions are imposed on both equations for the vertical boundaries in [1 1 0]. All simulations are carried out using an efficient spectral-Galerkin method for the 3D high-order equations.[43]

The shadowing growth of A-TiO_2 nanorods under low-pressure CVD is simulated. For $M/|\vec{R}| \geq 1$, conformal growth is observed. Promoted by the domination of surface diffusion, the late-stage morphology converges to a faceted nanorod terminated by facets corresponding to the minima of $\gamma(\boldsymbol{n})$. This result is equivalent to the Wulff shape constrained to surfaces belonging to the [1 1 0] zone.

Figure 4 shows the morphology of the nanorod at late-stage of growth with $M/|\vec{R}| = 1$. The facets are colored according to the IPF stereographic triangle in Fig. 3. For a more comprehensive representation of the facet distribution, surface pole figures are also shown for the surface area with intensity in units of multiples of random distribution (MRD) referred to the (110) pole aligned to the long axis of the simulation cell along the primary growth direction [1 1 0] of the A-TiO_2 nanorod. {110}, {112}, and {116} planes can be identified on the surface pole figure with {112} planes predominating the surface area. No side branches or plates are formed due to the rapid surface diffusion.

An intermediate dendritic morphology is obtained for $M/|\vec{R}| = 0.1$, as shown in Fig. 5. The surface diffusion in this case is less effective, which allows for surface modulation and the breakups of the {112} facets (yellow). It is worth noting that facet splitting is a feature of the morphological development only present when the surface diffusion is finite.[38,44] The onset of facet splitting occurs around $M/|\vec{R}| = 0.1$, and it is more pronounced as the effect of surface diffusion is reduced. More kinetically favored facets are formed for $M/|\vec{R}| \leq 0.1$. Due to the antipodal symmetry for both $M/|\vec{R}| = 1$ and $M/|\vec{R}| = 0.1$, only the upper pole figure is shown. For $M/|\vec{R}| = 0.01$, however, this symmetry is broken.

For a more limited surface diffusion, $M/|\vec{R}| = 0.01$, the resulting morphology exhibits the twofold rotational symmetry about ⟨110⟩ of the 4/mmm point group, as opposed to the fourfold symmetry about ⟨110⟩ for the equilibrium shape as well as in the cases of $M/|\vec{R}| = 1$ and $M/|\vec{R}| = 0.1$. Accompanying the breaking of symmetry, kinetically frozen plate-like structures emerge. These secondary structures are bounded predominately by the out-of-equilibrium {116} facets, indicated by the high intensity near the {116} poles on the surface pole figure in Fig. 6. {116}-facets have been previously reported in the synthesis of A-TiO_2 nanosheets with superior electrochemical properties.[45] Unlike our model-based approach, the {116} exposed surfaces are indirectly identified by the enhanced peaks of the orthogonal planes of {116}, e.g., (220) and (211), in XRD.

Figure 7(a) shows a rotated view of the simulated structure in Fig. 6, and Fig. 7(b) shows an SEM image of three A-TiO_2 nanorods separated from a titania thin film with a ⟨110⟩ texture (out-of-plane orientation). In the SEM image, the in-plane orientations for the three nanorods are different with the middle one orientated approximately 90° to the two adjacent ones. The model result in Fig. 7(a) is plotted in an orientation corresponding to the left nanorod highlighted on the SEM image in (b). Grooves in between the secondary plates in (b) are observed, which are common for systems with small surface diffusion.[30,32] The secondary plates are well-aligned and tilted at an angle with respect to the fastest growth direction of the thin film, i.e., [1 1 0]. This yields theoretically a 29° angle between $\vec{n}_{\{112\}}$ and ⟨110⟩. However, the average tilt axis of the secondary structures is a little off the axis of $\vec{n}_{\{112\}}$ because $\angle(\vec{n}_{\{112\}}, \vec{n}_{\{116\}}) = 91.3°$, and they are not fully faceted by {116} planes alone, evident in the intensity spread around {116} poles in Fig. 7.

The average inclination, β', of the secondary plates can be directly measured on the plot of dimensionless crystallinity defined by

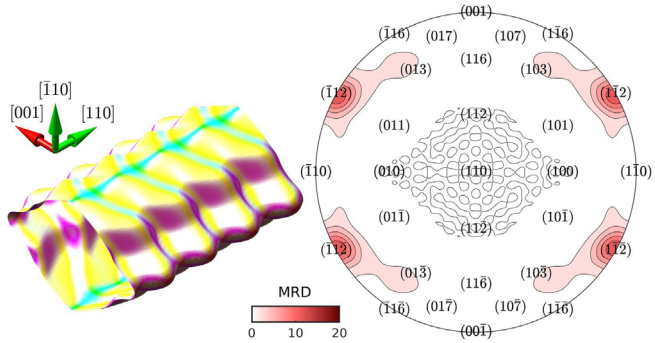

FIG. 5. A-TiO_2 nanorod morphology obtained with $M/|\vec{R}| = 0.1$. Four {112} poles indicate an abundance of exposed facets of {112}-type demonstrating the onset of facet-splitting.

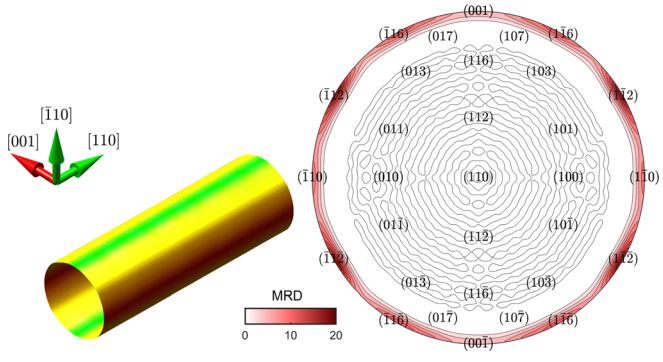

FIG. 4. A-TiO_2 nanorod morphology obtained with mobility to flux ratio $M/|\vec{R}| = 1$.

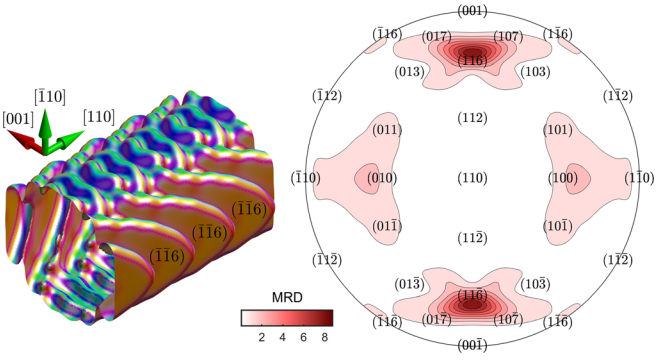

FIG. 6. Nanorod morphology obtained for $M/|\vec{R}| = 0.01$. The upper pole figure is superimposed with the lower for this morphology.

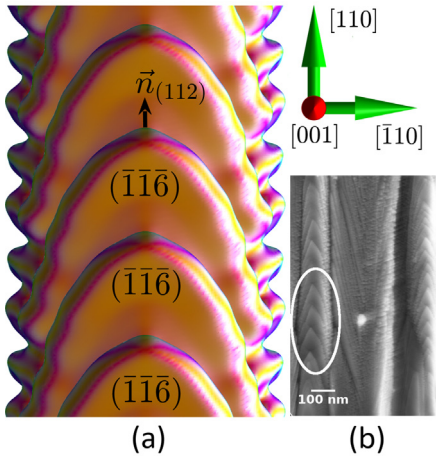

FIG. 7. (a) Rotated view of the A-TiO_2 nanorod from Fig. 6 viewed into the [001] zone axis, corresponding to the SEM image (b) adapted from our previous experimental work.[10]

$(1-\phi)^2/max[(1-\phi)^2]$, Fig. 8. We use the notation $\langle 112 \rangle$ to describe orientation of the faceted structures that give rise to the most abundant {116} facets. The model-based characterization points to an average tilt angle β' amounting to 26.5°, as annotated on the plot in Fig. 8. This result is in line with reported TEM images,[7–9] in which the tilt angle can be measured. It should be noted here that the measurement of the average tilt angle using TEM images is subject to errors due to the misalignment of the zone axis with the thin film orientation.

The $M/|\vec{R}|$ parameter in the model, which is effectively the balance of competition between the stabilizing diffusive effect and the destabilizing local shadowing growth, is responsible for the selection of $\langle 112 \rangle$. It can be seen as a crucial property of the titania thin film material, as far as the photoconductive applications are concerned. The abundance of highly active {116} facets is a consequence of the development of the $\langle 112 \rangle$ growth direction, which the authors are not aware of any direct experimental characterization of it.

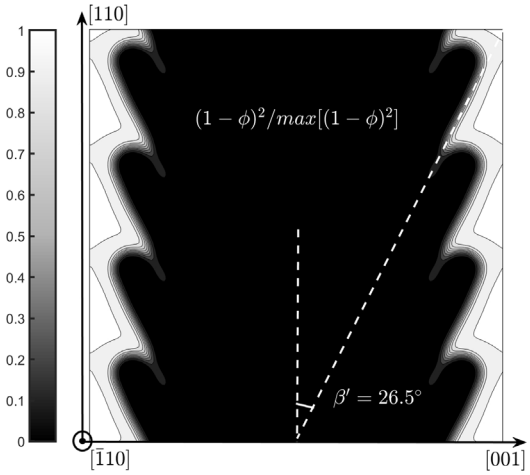

FIG. 8. Dimensionless crystallinity of the A-TiO_2 nanorod morphology viewed into the [$\bar{1}$10] zone axis.

The results of our simulations with limited surface diffusion $M/|\vec{R}| = 0.01$ are consistent with experimental results for low pressure CVD-grown columnar films even though gas phase reactions and surface decomposition are not included in our model. This suggests that the rate of surface reactions is rapid in comparison to the rate of ad-species surface mobility. Our work further suggests that if $M/|\vec{R}|$ can be increased, potentially by increasing the temperature or lowering the pressure in the low pressure CVD growth regime, then different dendritic structures could be developed: compare Fig. 4 with Fig. 6. Furthermore, the results reported here are constrained to a specific set of *a priori* identified facets. Additional surfaces could be included in the calculation as long as surface energies were determined. Then processing routes to optimize the exposed surfaces, either over the specific surface area or for specific high photocatalytically active facets, could be designed.

We report a complete characterization of these well-aligned structures observed on the A-TiO_2 nanorod. Anisotropic interfacial energies, adparticle attachment physics, and finite diffusivity are considered in 3D simulations of shadowing growth. Crystallography, tilt angles, and growth directions for the characteristic secondary, platelike facets are evaluated through the analysis. The {116}-type exposed surface has been identified, and dendritic nanorod morphology with grooves is obtained. These are crucial properties in the design and fabrication of the thin film that have not been previously captured by direct experimental techniques. Our characterizations are in agreement with indirect microscopy results in the literature.

The method also demonstrates promising future applications in characterizing surface morphologies of general nanostructured thin films. The material-specific model and its implementation can be easily modified to facilitate the study of other materials of interest with different surface energies. Flexibility in the process-specific model allows for adaption to more sophisticated vapor phase transport informed by, e.g., direct simulation Monte Carlo.

This work was supported in part by the New Zealand Ministry for Business Innovation and Employment (MBIE) under Grant No. CONT-42986-HVM.

AUTHOR DECLARATIONS

Conflict of Interest

The authors have no conflicts to disclose.

DATA AVAILABILITY

The data that support the findings of this study are available from the corresponding author upon reasonable request.

REFERENCES

[1]A. Wasa, J. G. Land, R. Gorthy, S. Krumdieck, C. Bishop, W. Godsoe, and J. Heinemann, FEMS Microbiol. Lett. **368**, 39 (2021).
[2]S. Krumdieck, R. Gorthy, J. G. Land, A. J. Gardecka, M. I. J. Polson, R. Boichot, C. M. Bishop, and J. V. Kennedy, Phys. Status Solidi (a) **215**, 1700578 (2018).
[3]C. A. Chen, Y. M. Chen, K. Y. Chen, J. K. Chi, Y. S. Huang, and D. S. Tsai, J. Alloys Compd. **485**, 524 (2009).
[4]S. S. Mali, J. V. Patil, and C. K. Hong, *Nanomaterials for Solar Cell Applications* (Elsevier, 2019), p. 349.

[5]J. Lee, T. Lee, P. Yoo, M. Grätzel, S. Mhaisalkar, and N. Park, J. Mater. Chem. A **2**, 9251 (2014).
[6]S. H. Nam, J. S. Hyun, and J. H. Boo, Mater. Res. Bull. **47**, 2717 (2012).
[7]R. S. Chen, C. A. Chen, H. Y. Tsai, W. C. Wang, and Y. S. Huang, Appl. Phys. Lett. **100**, 123108 (2012).
[8]C. Chen, Y. Chen, Y. Huang, D. Tsai, K. Tiong, and P. Liao, CrystEngComm **11**, 2313 (2009).
[9]A. J. Gardecka, M. Polson, S. P. Krumdieck, Y. Huang, and C. M. Bishop, Thin Solid Films **685**, 136 (2019).
[10]S. P. Krumdieck, R. Boichot, R. Gorthy, J. G. Land, S. Lay, A. J. Gardecka, M. Polson, A. Wasa, J. E. Aitken, J. A. Heinemann, G. Renou, G. Berthomé, F. Charlot, T. Encinas, M. Braccini, and C. M. Bishop, Sci. Rep. **9**, 1883 (2019).
[11]S. C. Jung and N. Imaishi, Korean J. Chem. Eng. **18**, 867 (2001).
[12]S. C. Jung, S. J. Kim, N. Imaishi, and Y. I. Cho, Appl. Catal. B **55**, 253 (2005).
[13]R. Chen, Y. Liu, C. Chan, and Y. Huang, Appl. Phys. Lett. **105**, 153107 (2014).
[14]J. Wu and C. Yu, J. Phys. Chem. B **108**, 3377 (2004).
[15]L. Meng, T. Ren, and C. Li, Appl. Surf. Sci. **256**, 3676 (2010).
[16]J. Augustynski, Electrochim. Acta **38**, 43 (1993).
[17]T. Luttrell, S. Halpegamage, J. Tao, A. Kramer, E. Sutter, and M. Batzill, Sci. Rep. **4**, 4043 (2014).
[18]Z. Yin, S. B. Betzler, T. Sheng, Q. Zhang, X. Peng, J. Shangguan, K. C. Bustillo, J. Li, S. Sun, and H. Zheng, Nano Energy **62**, 507 (2019).
[19]W. Yu, H. J. Fu, T. Mueller, B. S. Brunschwig, and N. S. Lewis, J. Chem. Phys. **153**, 020902 (2020).
[20]D. Astruc and F. Chardac, Chem. Rev. **101**, 2991 (2001).
[21]X. Gao, Y. Zhou, D. Han, J. Zhou, D. Zhou, W. Tang, and J. Goodenough, Joule **4**, 1864 (2020).
[22]R. Gorthy, S. Krumdieck, and C. Bishop, Materials **13**, 1668 (2020).
[23]Y. Huang, "Continuum model for nanocolumn growth during low-pressure vapour deposition," PhD dissertation (University of Canterbury, 2019).
[24]L. Abelmann and C. Lodder, Thin Solid Films **305**, 1 (1997).
[25]F. Tang, G. C. Wang, and T. M. Lu, J. Appl. Phys. **102**, 014306 (2007).
[26]C. Gaire, P. Snow, T. Chan, W. Yuan, M. Riley, Y. Liu, S. B. Zhang, G. C. Wang, and T. M. Lu, Nanotechnology **21**, 445701 (2010).
[27]S. Lichter and J. Chen, Phys. Rev. Lett. **56**, 1396 (1986).
[28]R. Karunasiri, R. Bruinsma, and J. Rudnick, Phys. Rev. Lett. **62**, 788 (1989).
[29]J. Yao and H. Guo, Phys. Rev. E **47**, 1007 (1993).
[30]G. S. Bales and A. Zangwill, J. Vac. Sci. Technol. A **9**, 145 (1991).
[31]D. Paritosh, J. Appl. Phys. **91**, 1963 (2002).
[32]M. Salvalaglio, R. Backofen, and A. Voigt, Phys. Rev. B **94**, 235432 (2016).
[33]M. Salvalaglio, R. Backofen, R. Bergamaschini, F. Montalenti, and A. Voigt, Cryst. Growth Des. **15**, 2787 (2015).
[34]Y. Huang, S. L. Masters, S. P. Krumdieck, and C. M. Bishop, J. Appl. Phys. **128**, 55303 (2020).
[35]M. Pelliccione and T. M. LU, Mod. Phys. Lett. B **21**, 1207 (2007).
[36]A. Yanguas-Gil, J. Cotrino, A. Barranco, and A. Gonzalez-Elipe, Phys. Rev. Lett. **96**, 236101 (2006).
[37]T. M. Lu, Y. P. Zhao, J. T. Drotar, T. Karabacak, and G. C. Wang, MRS Proc. **749**, 1 (2002).
[38]A. van der Drift, Philips Res. Rep. **22**, 267–288 (1967).
[39]S. Torabi and J. Lowengrub, Phys. Rev. E **85**, 041603 (2012).
[40]M. Salvalaglio, R. Backofen, A. Voigt, and F. Montalenti, Nanoscale Res. Lett. **12**, 552 (2017).
[41]M. Salvalaglio, R. Bergamaschini, R. Backofen, A. Voigt, F. Montalenti, and L. Miglio, Appl. Surf. Sci. **391**, 33 (2017).
[42]T. Ohno, K. Sarukawa, and M. Matsumura, New J. Chem. **26**, 1167 (2002).
[43]F. Chen and J. Shen, J. Comput. Phys. **231**, 5016 (2012).
[44]Paritosh and D. Srolovitz, J. Appl. Phys. **91**, 1963 (2002).
[45]F. Li, X. Li, R. Peng, X. Zhai, S. Yang, Z. Fu, and Y. Lu, Nanoscale **6**, 12434 (2014).